Toward Spectral-Domain Optical Coherence Tomography on a Chip

B. Imran Akca, Van Duc Nguyen, Jeroen Kalkman, Nur Ismail, Gabriel Sengo, Fei Sun, Alfred Driessen, Ton G. van Leeuwen, Markus Pollnau, Kerstin Wörhoff, and René M. de Ridder, *Member, IEEE*

***Abstract*—We present experimental results of a spectral-domain optical coherence tomography system based on an integrated optical spectrometer. A 195-channel arrayed-waveguide-grating (AWG) spectrometer with 0.4-nm channel spacing centered at 1300 nm and a 125-channel AWG with 0.16-nm channel spacing centered at 800 nm have been fabricated in silicon oxynitride waveguide technology. Interferometric distance measurements have been performed by launching light from a broadband source into a free-space Michelson interferometer, with its output coupled into the AWG. A maximum imaging depth of 1 mm and axial resolution of 25 and 20 μm in air are demonstrated for the 800- and 1300-nm ranges, respectively.**

***Index Terms*—Arrayed waveguide grating (AWG), optical coherence tomography (OCT), optical waveguides, silicon oxynitride (SiON), spectrometer.**

I. Introduction

OPTICAL coherence tomography (OCT) [1] is a noninvasive optical technique for high-resolution cross-sectional imaging of biological tissue, with many applications in clinical medicine. The measurement principle of OCT is based on low-coherence interferometry (LCI) in which interference patterns due to the superposition of a multitude of waves with a large spread in wavelengths are studied. These distinctive patterns enable one to determine the location at which light is reflected back and to measure the depth profile of the scattering amplitude. By performing multiple LCI measurements at different lateral coordinates on a sample, a 3-D cross-sectional image of the scattering amplitude can be constructed.

Current state-of-the-art OCT systems operate in the Fourier domain, using either a broadband light source and a spectrometer, known as "spectral-domain OCT" (SD-OCT), or a rapidly tunable laser, known as "swept-source OCT" (SS-OCT). Fourier-domain OCT (FD-OCT) systems (SS-OCT and SD-OCT) were invented by Fercher *et al*. in 1995 [2]. However, FD-OCT gained wide acceptance only after nearly ten years, when it was realized that FD-OCT offered a significant sensitivity advantage over time-domain OCT. SS-OCT systems are advantageous for their simple single-element detection and better sensitivity with imaging depth (lower sensitivity roll-off), but they typically have lower axial resolution compared to SD-OCT and suffer from phase instability. In addition, they require a more expensive light source. SD-OCT systems can utilize simple broadband sources; however, they suffer from severe signal roll-off in depth and require more complicated detection optics, i.e., line scan cameras and spectrometers [3]. Ultrahigh axial resolution of 2.1–3.5 μm in the retina from 10 to 29 kHz axial scan rates were demonstrated with SD-OCT systems [4]–[6]. Recently, by using high-speed CMOS cameras in retinal imaging, an axial scan rate of 312 kHz was obtained with an axial resolution of 8–9 μm in the 850-nm spectral range [7]. Current commercial SD-OCT systems typically achieve $\sim$5 μm axial resolution with $\sim$25–27 kHz axial scan rates over an imaging range of $\sim$2.0–2.6 mm. The fastest speed in retina imaging was demonstrated by Fujimoto *et al*. at 100 000–400 000 axial scans per second with an axial resolution of 5.3 μm, using a 1050-nm SS-OCT system [8]. Although current SS-OCT systems seem to perform better than SD-OCT systems due to the improved light sources, SD-OCT systems have been used quite extensively for polarization sensitive OCT, Doppler OCT, ultrawide-bandwidth OCT, ultrahigh-resolution OCT and, moreover, they represent the state of the art in commercial ophthalmologic OCT systems [3]. Both systems contain a multitude of fiber and free-space optical components that make these instruments costly and bulky. The size and cost of an OCT system can be decreased significantly by the use of integrated optics. A suitable material technology and optimum design may allow one to fabricate extremely compact and low-cost OCT systems. In addition, integrated optics can enhance the performance of OCT by, for example, parallelization [9], [10] of OCT devices on a chip.

Only limited data on the implementation of OCT components on a chip exists. Culemann *et al*. [11] fabricated an integrated optical sensor chip in ion-exchanged low-index-contrast glass

Manuscript received May 14, 2011; revised September 13, 2011 and October 4, 2011; accepted October 5, 2011. Date of publication October 13, 2011; date of current version June 1, 2012. This work was supported by the Smart Mix Program of the Netherlands Ministry of Economic Affairs and the Netherlands Ministry of Education, Culture and Science, and by the Dutch Senter-Novem Merging Electronics and Micro and Nano Photonics in Integrated Systems Project.

B. I. Akca, N. Ismail, G. Sengo, A. Driessen, M. Pollnau, K. Wörhoff, and R. M. de Ridder are with the Integrated Optical MicroSystems Group, MESA+ Institute for Nanotechnology, University of Twente, 7500 AE Enschede, The Netherlands (e-mail: B.I.Akca@utwente.nl; N.Ismail@utwente.nl; G.Sengo@utwente.nl; A.Driessen@utwente.nl; M.Pollnau@utwente.nl; k.worhoff@utwente.nl; R.M.deRidder@utwente.nl).

V. Duc Nguyen and J. Kalkman are with the Department of Biomedical Engineering and Physics, Academic Medical Center, University of Amsterdam, NL-1100 DE Amsterdam, The Netherlands (e-mail: d.v.nguyen@amc.uva.nl; J.Kalkman@amc.uva.nl).

F. Sun is with the Institute of Microelectronics, A*STAR, 117685, Singapore (e-mail: F.Sun@utwente.nl).

T. G. van Leeuwen is with the Biomedical Photonic Imaging Group, MIRA Institute for Biomedical Technology and Technical Medicine, University of Twente, 7500 AE Enschede, The Netherlands, and also with the Department of Biomedical Engineering and Physics, Academic Medical Center, University of Amsterdam, NL-1100 DE Amsterdam, The Netherlands (e-mail: t.g.vanleeuwen@amc.uva.nl).

Color versions of one or more of the figures in this paper are available online at http://ieeexplore.ieee.org.

Digital Object Identifier 10.1109/JSTQE.2011.2171674

for time-domain OCT, with all other components external to the optical chip. Margallo-Balbas *et al*. realized a rapidly scanning delay line in silicon—based on the thermo-optic (TO) effect of silicon—for application in time-domain OCT, operating at line rates of 10 kHz and a scan range of nearly 1 mm [12]. Yurtsever *et al*. [13] demonstrated a silicon-based Michelson interferometer (MI) for a SS-OCT system with 40 μm of axial resolution and a sensitivity of 25 dB, both insufficient for imaging. Nguyen *et al*. [14] demonstrated integrated elliptic couplers and applied them to Fizeau-based spectral-domain low-coherence depth ranging. Choi *et al*. were the first to demonstrate the performance of an arrayed-waveguide-grating (AWG) spectrometer in an SD-OCT system with a depth range of 3 mm and an axial resolution of 23 μm. However, they needed semiconductor optical amplifiers in order to obtain sufficient sensitivity for imaging [15]. Recently, we have demonstrated a depth range of 1 mm and an axial resolution of 19 μm by performing interferometric distance measurements in a fiber-based SD-OCT system with a silicon-oxynitride (SiON)-based AWG designed for the 1300-nm wavelength range [16].

One of the key components of an SD-OCT system is the high-resolution spectrometer (spectrometers also have been employed in SS-OCT to reduce motion artifacts [17]). Although integration of a spectrometer on a chip is challenging, AWGs present a well established way toward miniaturization. AWGs are used for wavelength (de)multiplexing in telecommunication, offering high resolution over a small bandwidth [18]. AWGs are ideally suited for applications such as OCT and spectroscopy, with their high spectral resolution, small form factor, large bandwidth, and low insertion loss [19]. In addition to their advantages listed previously, AWGs are cost effective, which makes them favorable for integration with SD-OCT systems. However, there are design limitations on resolution and free spectral range (FSR), which restrict the axial resolution and maximum imaging range of SD-OCT systems. By applying different approaches (e.g., cascading several AWGs and compensating the inherent additional loss by increasing the power of the light source), these limitations can be overcome.

SiON is a promising material for AWG spectrometer applications. Its refractive index can be chosen between the values of silicon dioxide (1.45) and silicon nitride (2.0), thus, allowing for a flexible waveguide design [20]. A small bending radius down to several micrometers can be obtained by using the highest refractive index contrast with a proper waveguide geometry. Furthermore, SiON is transparent in a broad wavelength range from 210 nm to beyond 2000 nm [21], so that AWGs can be fabricated for both the visible and infrared wavelength ranges by use of the same material system; in specific cases, even the same AWG structure could be used for both regions. In the literature, there is only limited data on SiON-based AWG spectrometers [22]–[27]. Schauwecker *et al*. reported the smallest AWG on the SiON platform, with an overall chip size of 5 mm $\times$ 2 mm [22]. The fiber-to-chip coupling loss of a 32-channel, 100-GHz spacing AWG has been reduced significantly with integrated spot-size converters [23]. The largest FSR was reported by Shimoda *et al*. [24]. Their AWG showed 2-nm channel spacing, 80-nm FSR, and 2.2-dB insertion loss.

In this paper, we present two SiON-based AWG spectrometers for the spectral ranges near 800 and 1300 nm, which are aimed to be used as integrated spectrometers in future fully integrated SD-OCT systems. We investigate the performance of integrated SiON-based AWG spectrometers with high resolution and large FSR in interferometric depth ranging and OCT imaging, thereby demonstrating the first important step toward miniaturization of an SD-OCT system.

II. Design and Realization

A. Essential OCT Parameters

The essential parameters that determine the imaging quality of FD-OCT systems are center wavelength, axial resolution, maximum imaging depth, signal-to-noise ratio (SNR), and sensitivity roll-off in depth.

First, the OCT imaging depth is limited by the amount of scattering (higher at shorter wavelengths) and absorption (higher at longer wavelengths) in biological tissue. Therefore, the OCT imaging depth depends on the choice of center wavelength of the OCT system. In this paper, two common OCT wavelengths (λ_c) are used, 800 nm for imaging ophthalmic structures where water absorption is dominant and 1300 nm for dermal imaging where scattering is dominant.

Second, the axial resolution of an SD-OCT system is determined by the effective bandwidth of the light that is detected. It depends on both the bandwidth of the light source and the bandwidth of the spectrometer. If the spectrum of the light source, as measured with the spectrometer, has a Gaussian envelope with full-width at half-maximum (FWHM) $\Delta\lambda_{\mathrm{FWHM}}$, the axial (depth) resolution Δz is given by [28]

$$\Delta z = \frac{2\ln 2}{\pi n}\left(\frac{\lambda_c^2}{\Delta\lambda_{\mathrm{FWHM}}}\right) \tag{1}$$

where n is the (group) refractive index of the imaged tissue.

Third, the maximum imaging depth $z_{\max}$ in SD-OCT is determined by the spectral sampling interval (δk, k is the wave number). From Nyquists's sampling theorem, the spectral sampling at δk spacing leads to a maximum path length of $1/(2\delta k)$. However, since every path length corresponds to half the depth (light travels back and forth to the detector), the imaging depth becomes $1/(4\delta k)$. Considering the wavenumber-to-wavelength conversion, it becomes [29]

$$z_{\max} = \frac{\lambda_c^2}{4n\delta\lambda} \tag{2}$$

where $\delta\lambda$ is the wavelength resolution of the spectrometer.

Fourth, the roll-off in depth of the SD-OCT signal is determined by the spectral content of the spectrometer and the camera pixel size. The imaging range of SD-OCT is limited by the signal roll-off, which is the attenuation of the OCT signal due to washout of the interference fringe visibility with increasing depth. The signal amplitude roll-off function is given by [30]

$$A(z) = \frac{\sin(d_x Rz)}{(d_x Rz)}\exp\left[-\frac{a^2R^2z^2}{4\ln 2}\right] \tag{3}$$

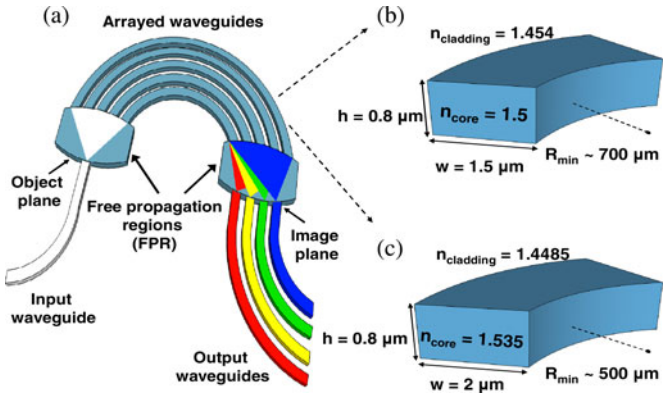

Fig. 1. (a) Schematic layout of an AWG. Channel waveguide geometry for (b) the AWG centered at 800 nm and (c) the AWG centered at 1300 nm.

where d_x is the pixel width, R is the reciprocal linear dispersion of the spectrometer ($\delta k/d_x$), and a is the spot size. The Sinc and Gaussian functions in (3) correspond to the Fourier transform of the square-shaped camera pixels and Gaussian beam profile in the spectrometer, respectively. By applying wavenumber-to-wavelength conversion, (3) becomes

$$A(z) = \frac{\sin\left((2\pi\delta\lambda/\lambda^2)z\right)}{(2\pi\delta\lambda/\lambda^2)z} \exp\left[-\frac{\pi^2}{\ln 2}\left(\frac{a\delta\lambda z}{\lambda^2 d_x}\right)^2\right]. \quad (4)$$

Rearranging (4) by using (2) yields

$$A(z) = \frac{\sin(\pi z/2z_{\max})}{(\pi z/2z_{\max})} \exp\left[-\frac{\pi^2}{16\ln 2}\left(\frac{a}{d_x}\right)^2\left(\frac{z}{z_{\max}}\right)^2\right]. \quad (5)$$

$z_{\max}$ is taken from (2) and (a/d_x) is defined as ω in [31], which is the ratio of the spectrometer FWHM spectral resolution to the wavelength resolution.

Finally, for maximum SNR, the spectrometer loss should be minimized in the design stage. Typical SNR values for high-quality OCT imaging are on the order of 100 dB [3], [4], [30].

B. AWG Operation

The operation of an AWG [18] is briefly explained, referring to Fig. 1(a). Light from an input waveguide diverges in a first free propagation region (FPR) in order to illuminate the input facets of an array of waveguides with a linearly increasing length. For a central wavelength λ_c, the phase difference at the output facets of adjacent array waveguides is an integer multiple of 2π. Since these facets are arranged on a circle, a cylindrical wavefront is formed at the beginning of a second FPR, which generates a focal spot at the central output channel. Since the phase shift caused by the length differences between arrayed waveguides is linearly dependent on wavelength, the resulting wavelength-dependent phase gradient implies a tilt of the cylindrical wavefront at the beginning of the second FPR, which causes the focal spot to shift with wavelength to different output waveguides.

C. AWG Parameters for OCT Imaging

The axial resolution of an SD-OCT system using an AWG is determined by the effective bandwidth of the detected spectrum, which depends on both the bandwidth of the light source and the FSR of the spectrometer. Matching the bandwidth of the AWG transmission function with the bandwidth of the light source is the most economical configuration, since for a given source bandwidth, the axial resolution will not improve if the bandwidth of the AWG transmission function is made much larger than this bandwidth, and vice versa. The maximum value of the transmission bandwidth of an AWG is its FSR, which is valid for loss uniformity ≤ -3 dB. In practice, the FSR of an AWG is limited by the size of the device. In this paper, the FSR values of our AWG spectrometers are chosen to be 20 and 78 nm for $\lambda_c = 800$ and 1300 nm, respectively, by considering the design limitations. The bandwidths of the light sources that we used in the OCT measurements are much smaller than the bandwidths of the AWG spectrometers: $\Delta\lambda_{\mathrm{FWHM}} = 13$ and 40 nm, respectively. In this way, the axial resolution is mainly determined by the bandwidth of the light source. According to (1), the bandwidths of the chosen light sources limit the theoretical axial resolution (for air, $n = 1$) to $\Delta z = 23$ and 18.5 μm for $\lambda_c = 800$ and 1300 nm, respectively. In tissue ($n \sim 1.33$), the aforementioned axial resolutions become 17 and 14 μm, respectively. With a proper light source (larger bandwidth) and an AWG with a larger FSR (smaller grating order), the current axial resolution values can be improved to the level of existing OCT systems.

For both spectral ranges, we aim at a maximum depth range of $z_{\max} = 1$ mm, which according to (2) requires a wavelength spacing of $\delta\lambda = 0.16$ and 0.4 nm for the 800- and 1300-nm AWG, respectively. The choice for 1-mm imaging depth is a compromise between various imaging performance parameters. Given a fixed size of the AWG imaging plane, a larger imaging depth can be obtained when using an AWG with higher resolution; however, this would result in a lower optical bandwidth and lower spatial OCT resolution. Smaller spacing between adjacent waveguides results in an increased crosstalk and, consequently, more signal roll-off in depth.

For an SD-OCT system with an AWG spectrometer, the roll-off in depth is determined by the spectral content of the AWG output channels. Due to dispersion in the second FPR, the spectral content is limited by the size of the output waveguides. However, the spectral content in a single output waveguide can be increased due to diffraction-limited focusing of the light onto the output channel, crosstalk between output waveguides, and fabrication imperfections. For an AWG-based SD-OCT system, light is sampled twice; first at the focal plane of the AWG due to discretely located output waveguides and second at the camera pixels. The first sampling due to AWG output channels adds an extra Sinc term to (5), which is the Fourier transform of the rectangular-shaped output waveguides. In the extra Sinc term, caused by the AWG sampling, d_x is the tapered output waveguide width w_o and the reciprocal linear dispersion is defined as $\delta k/d_o$, where d_o is the spacing between adjacent output waveguides. By inserting the AWG parameters into the Sinc term of

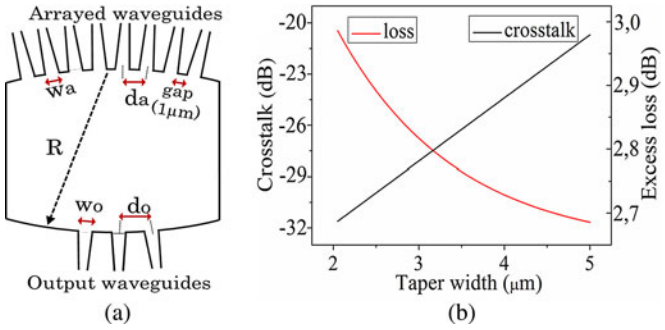

Fig. 2. (a) Geometry of the receiver side of the AWG (second FPR) and definition of parameters w_a, d_a, w_o, d_o, and R (see Table I). (b) Adjacent crosstalk and excess loss versus output taper width w_o.

(3) and following the same conversions, the final formula of the extra Sinc term becomes

$$\frac{\sin(w_o/d_o)(\pi z/2z_{\max})}{(w_o/d_o)(\pi z/2z_{\max})}. \tag{6}$$

By inserting (6) into (5), the modified formula of sensitivity roll-off is obtained

$$A(z) = \left[\frac{\sin(k\pi z/2z_{\max})}{(k\pi z/2z_{\max})}\right]\left[\frac{\sin(\pi z/2z_{\max})}{(\pi z/2z_{\max})}\right] \times \exp\left[-\frac{\pi^2\omega^2}{16\ln 2}\left(\frac{z}{z_{\max}}\right)^2\right] \tag{7}$$

where $k = w_o/d_o$ is the ratio of the width of the output waveguide to the separation between them at the focal plane of the AWG [see Fig. 2(a)]. Both AWG spectrometers are designed with $k = 0.5$. In order to avoid severe signal roll-off in depth, ω is chosen smaller than 1, which necessitates an adjacent-channel crosstalk value of less than -10 dB. The desired crosstalk value is achieved by setting the spacing between the output waveguides in the focal plane of the AWG spectrometers accordingly. The expected lower limit of ω is calculated with the simulated FWHM spectral resolution of the spectrometer and results in $\omega = 0.32$ and 0.55 for the 800- and 1300-nm AWG, respectively.

For maximum SNR, the AWG spectrometer loss is minimized by applying linear tapers at the interfaces of arrayed and input/output waveguides with the FPRs, as demonstrated in Fig. 2(a). Ideally, the gaps near the FPR between arrayed waveguides should approach zero in order to capture more light and, thereby, reduce the excess loss. This would, however, result in extremely sharp features that cannot be accurately reproduced by our lithographic processes; therefore, the gap width was chosen to be 1 μm for the arrayed waveguides. The taper width of the input/output waveguides was determined as a compromise between loss and adjacent-channel crosstalk: the larger the taper width, the lower the excess loss and the higher the crosstalk, as shown in Fig. 2(b), which is the simulation result of a typical AWG spectrometer.

As crosstalk arises from evanescent coupling between output waveguides, it decreases with increasing spacing. However, this leads to increased device size and, therefore, needs to be carefully designed. Acceptable minimum spacings between the arrayed waveguides and between the output waveguides were found by simulating device behavior using the 2-D beam propagation method in order to have an excess loss value of $\leq$3 dB (for the central channels) and a crosstalk value of ≤ -20 dB. The simulation results of both devices confirm that our choice of taper width and waveguide spacing fulfills the aforementioned excess loss and crosstalk requirements (see Table II).

TABLE I
DESIGN PARAMETERS OF THE AWG SPECTROMETERS

Parameters	AWG @ 800 nm	AWG @ 1300 nm
Wavelength spacing ($\delta\lambda$)	0.16 nm	0.4 nm
Central wavelength (λ_c)	800 nm	1300 nm
Free spectral range (FSR)	20 nm	78 nm
Diffraction order (m)	40	17
Focal length (R)	11 mm	12 mm
Path length increment (ΔL)	21.8 μm	15 μm
Number of arrayed waveguides (M)	500	650
Number of output channels (N)	125	195
Height of waveguide core (h)	800 nm	800 nm
Width of waveguide core (w)	1.5 μm	2.0 μm
Refractive index of core layer	1.50	1.535
Refractive index of cladding layer	1.454	1.4485
Minimum bending radius	700 μm	500 μm
Spacing of arrayed waveguides (d_a)	6 μm	7 μm
Spacing of output waveguides (d_o)	8 μm	8 μm
Taper width of arrayed waveguides (w_a)	5 μm	6 μm
Taper width of input/output waveguides (w_o)	3 μm	4 μm
Length of linear taper	400 μm	200 μm

D. AWG Design and Simulations

For both spectrometers, single-mode SiON channel waveguides, with the parameters provided in Table I, were fabricated. As SiON is transparent over a broad wavelength range that covers all the frequently used OCT wavelength bands at 800, 1000, and 1300 nm, AWGs can be fabricated for all these wavelength ranges in the same material system. The size of each device is optimized by beam-propagation simulations, which resulted in chip areas of 2.6 cm $\times$ 2.1 cm and 3 cm $\times$ 2.5 cm for the 800- and 1300-nm AWG, respectively.

The given refractive index values of core and cladding layers are for TE polarization. For maximum compactness of the devices, the refractive index of the core layer was chosen as high as possible, as consistent with the single-mode condition and limitations of the fabrication process. Schematic representations of the channel waveguides at 800 and 1300 nm are shown in Fig. 1(b) and (c), respectively.

For the 800-nm AWG, at the central channels, a crosstalk of -35 dB and an excess loss (with respect to a curved waveguide) of 2.6 dB were calculated. At the outermost channels, these values are -27 and 5.35 dB, respectively. The 3-dB bandwidth was calculated as 0.052 nm. For the 1300-nm AWG, crosstalk values of -33 and -20 dB and excess loss values of 1.8 and 6.3 dB were simulated for the central and outermost channels, respectively. The 3-dB bandwidth was calculated as 0.22 nm. Using a typical material birefringence of 1.5×10^{-3}, the polarization-dependent wavelength shift was calculated with a 2-D beam

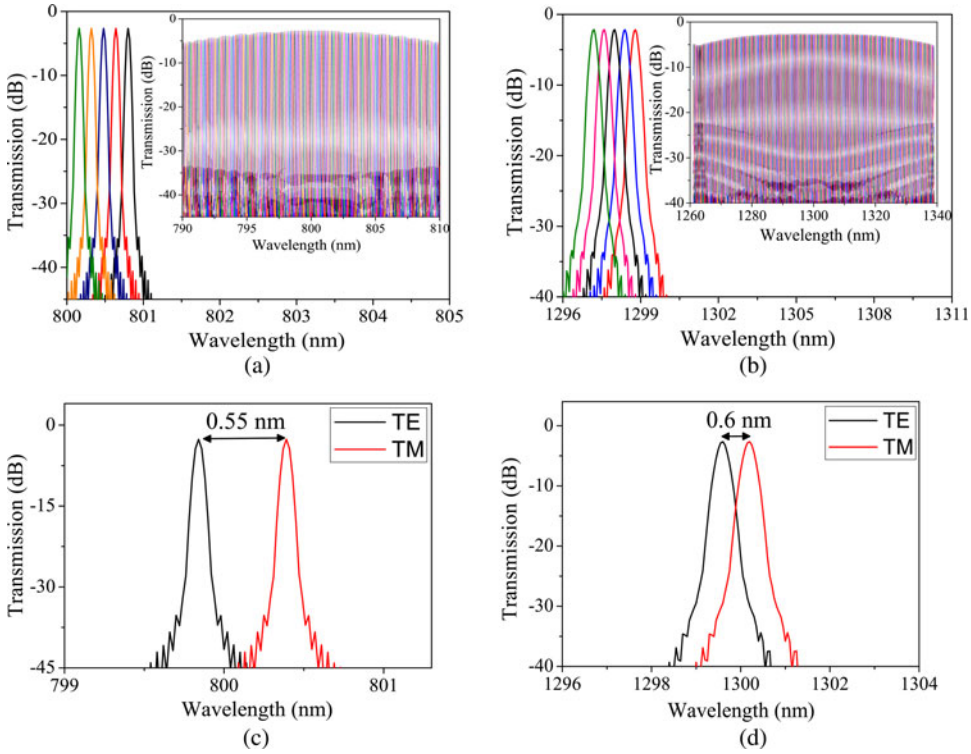

Fig. 3. AWG beam propagation simulation for TE-polarized light at the central channels for (a) the 800-nm AWG and (b) the 1300-nm AWG. The insets show the spectrum over the complete FSR of 20 and 78 nm, respectively. Simulation results for the polarization-dependent wavelength shift for (c) the 800-nm AWG and (d) the 1300-nm AWG.

TABLE II
MEASUREMENT AND SIMULATION RESULTS OF FABRICATED AWG SPECTROMETERS

Parameter		AWG @ 800 nm		AWG @ 1300 nm	
		Simulation	Measurement	Simulation	Measurement
Channel spacing (Δλ)		0.16 nm	0.16 nm	0.4 nm	0.4 nm
Free spectral range (FSR)		20 nm	19.4 nm	78 nm	77 nm
Polarization-dependent shift		0.55 nm	0.5 nm	0.6 nm	0.5 nm
Non-adjacent crosstalk	Center	-35 dB	-22 dB	-33 dB	-25 dB
	Outermost	-27 dB	-18 dB	-20 dB	-16 dB
Excess loss	Center	2.6 dB	3.2 dB	1.8 dB	2.5 dB
	Outermost	5.35 dB	6.5 dB	6.3 dB	8 dB
3-dB bandwidth		0.052 nm	0.07 nm	0.22 nm	0.23 nm

propagation method as 0.55 and 0.6 nm for the 800- and 1300-nm AWG, respectively. The simulation results and a summary of them are given in Fig. 3 and Table II, respectively.

E. Fabrication

The proposed AWGs were fabricated using plasma-enhanced chemical vapor deposition (PECVD), conventional photolithographic patterning, and reactive ion etching (RIE). The fabrication process flow is displayed in Fig. 4.

An 8-μm-thick oxide layer, serving as bottom cladding of the waveguides, was thermally grown on a Si substrate. A SiON core layer was deposited in a load-lock-equipped Oxford Plasmalab System 80 PECVD reactor at a substrate temperature of 300 °C, a chamber pressure of 86.66 Pa, and a power of 60 W (187.5 KHz). Silane (2% SiH_4 diluted in N_2) and nitrous oxide (N_2O) served as precursors in the deposition process. A relative gas-flow ratio N_2O/SiH_4 of 0.3 and 0.73 was used for the 1300- and 800-nm waveguide structures, respectively. The wavelength dispersion of the SiON refractive index was measured at three discrete wavelengths by prism coupling and fit to the Cauchy relation $n(\lambda) = A + B/\lambda^2$ with the Cauchy parameters of $A = 1.55$ and $B = 6.93 \times 10^{-3}$ μm^2.

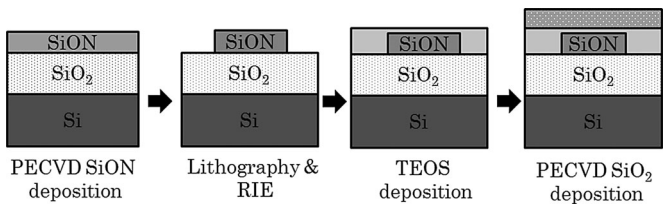

Fig. 4. Fabrication process flow of the AWG spectrometers and waveguides.

For definition of the waveguiding channels, a 500-nm-thick photoresist masking layer was spin-coated on top of the core

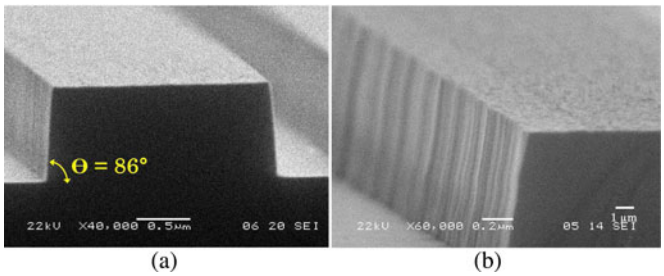

Fig. 5. SEM images of the test structures before top SiO_2 cladding deposition. (a) Sidewall angle (86°). (b) Sidewall roughness (≤40 nm).

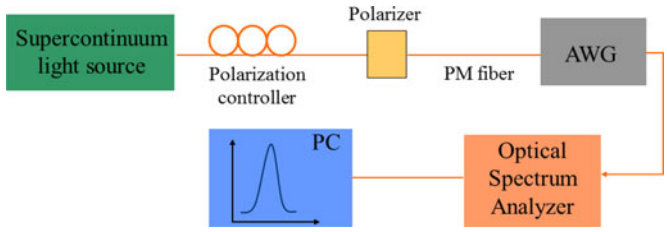

Fig. 6. Optical measurement setup used to characterize the AWG spectrometers.

layer. The waveguide pattern was defined in the photoresist layer with standard lithography and a development step. Then, the waveguiding channels were etched in a Plasma Therm 790 RIE reactor applying a gas mixture of CHF_3 and O_2 (100 sccm / 2 sccm) at 28 mTorr pressure, 350-W plasma power, and 20 °C temperature. Scanning electron microcopy (SEM) images of the test structures ($w = 2\,\mu$m and $h = 0.8\,\mu$m) before top oxide layer deposition are presented in Fig. 5.

After removal of the photoresist layer by developing, the upper cladding oxide layers were deposited in two steps. In order to obtain a conformal coverage of the channel waveguides, a 1-μm-thick oxide layer was first grown by low-pressure chemical vapor deposition using tetraethyl orthosilicate as precursor. Subsequently, a 3-μm-thick PECVD oxide layer was deposited to reach the designed thickness of the upper cladding. All deposition processes were followed by thermal annealing at 1150 °C for 3 h, for layer densification and stabilization of thickness and refractive index.

According to the SEM images, a sidewall roughness of ≤40 nm and a sidewall angle of 86° were obtained for both spectral ranges. The sidewall angle of 86° results in an effective refractive index difference of $\Delta n = 6.8 \times 10^{-4}$ and 8.3×10^{-4} between designed and fabricated devices, which corresponds to a center wavelength shift of 0.4 and 0.7 nm for the 800- and 1300-nm AWG, respectively.

III. AWG Characterization and Discussion

A. Optical Transmission Measurements

Optical transmission measurements were performed by coupling TE-polarized light from a supercontinuum light source (Fianium SC450) into the input waveguide with a single-mode polarization-maintaining fiber. The output signal was sent to an optical spectrum analyzer (iHR 550, Horiba Jobin Yvon) through a butt-coupled single-mode fiber. The schematic of the optical measurement setup is depicted in Fig. 6.

The complete FSR was measured by moving the fiber successively along all output channels (step and optimize transmission for each channel). Results were reproducible within ± 20%, the inaccuracy being mainly due to fiber-chip alignment errors. The transmission spectra measured at the output channels were normalized with respect to the transmission spectrum of a curved channel waveguide with the same radius and propagation length as the longest arrayed waveguide in the AWGs. The essential performance parameters are summarized in Table II for both AWGs. The calculated values are included in the table for comparison.

The measured transmission spectra of the central output waveguides of the 800-nm AWG are displayed in Fig. 7(a). The inset shows the complete set of 125 transmission spectra of the device. As predicted, each channel works as a bandpass wavelength filter. The measured values of resolution and FSR are consistent with the simulation results.

However, a 10-dB difference between the simulated and measured crosstalk values was found. The relatively high crosstalk is attributed mainly to phase errors due to nonuniformity of the refractive index and thickness of the core layer, which was a major problem for the devices that were fabricated after a failure of PECVD and RIE machines. In addition, a center wavelength shift of 1.2 nm was measured due to the same cause. For TM compared to TE polarization, we measured a central-wavelength shift of $\Delta\lambda = 0.5$ nm, corresponding to an effective refractive index difference between the two polarizations, i.e., the waveguide birefringence of

$$\Delta n = n_{\mathrm{TE}} - n_{\mathrm{TM}} = \frac{m\Delta\lambda}{\Delta L}. \tag{8}$$

With diffraction order $m = 40$ and path length increment $\Delta L = 21.8\,\mu$m, (8) yields $\Delta n \cong 0.9 \times 10^{-3}$.

Fig. 7(b) displays the measured transmission spectra of the central output waveguides of the 1300-nm AWG. The inset of Fig. 7(b) represents the complete set of 195 transmission spectra of the device. The measured values of resolution and FSR are consistent with the simulation results. An 8-dB difference between the calculated and measured crosstalk values and a center wavelength shift of 2 nm was found due to the same cause as explained previously for the 800-nm AWG. We observed a polarization-dependent shift of 0.5 nm for the central wavelength, which corresponds to an effective refractive index difference of $\sim 0.6 \times 10^{-3}$ between TE and TM polarizations according to (8).

For the AWGs at 800 and 1300 nm, we observed random differences between the peak values of the transmission spectra of the different output channels, arising from a limited reproducibility of the used measurement method. The optical transmission of each output channel was measured using a single butt-coupled fiber which had to be repositioned to the next channel after each measurement. Although the fiber-chip coupling efficiency was maximized each time, the intensity variations were not eliminated completely. However, for the OCT imaging

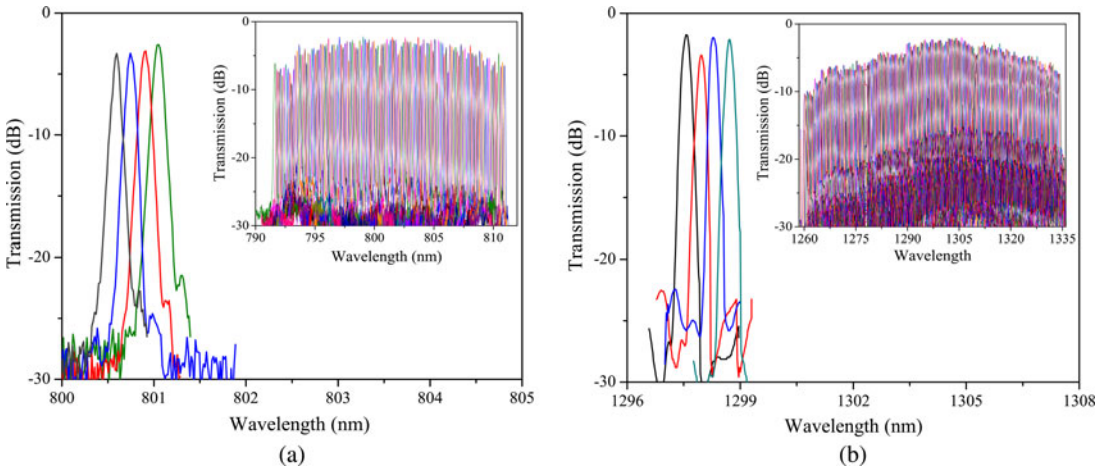

Fig. 7. AWG performance for TE-polarized light at the central channels for (a) the 800-nm AWG and (b) the 1300-nm AWG. The insets show the spectrum over the complete FSR of 19.4 and 77 nm, respectively. All spectra are normalized with respect to that of a curved reference waveguide.

TABLE III
EFFECTS OF TECHNOLOGICAL TOLERANCES ON AWG PERFORMANCE

Parameters	AWG @ 800 nm			AWG @ 1300 nm		
	Δn_{eff} ($\times 10^{-3}$)	$\Delta\lambda$ (nm)	$\Delta_{crosstalk}$ (dB)	Δn_{eff} ($\times 10^{-3}$)	$\Delta\lambda$ (nm)	$\Delta_{crosstalk}$ (dB)
$\Delta w = \pm 0.1$ µm	1.7	0.92	6	1.85	1.63	9
$\Delta n_{core} = \pm 3\times10^{-4}$	0.4	0.22	0.5	0.3	0.26	1.2
$\delta d_{core} = \pm 0.5$ %	1.97	1.07	8	3.6	3.18	14
$\Delta n_{cladding} = \pm 3\times10^{-4}$	0.12	0.06	0.4	0.17	0.15	0.7

measurements, the light coming out of the output channels will be imaged onto the camera by using free-space coupling, which eliminates fiber-chip-coupling-related problems completely.

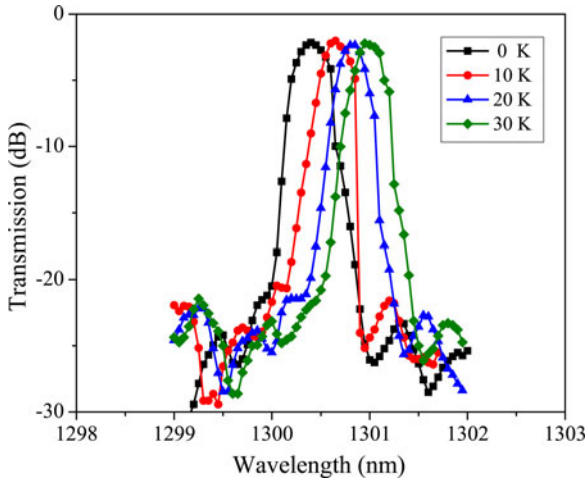

Fig. 8. Measured TO tuning characteristic of the 1300-nm AWG.

B. Tolerance Analysis

The AWG performance is affected mainly by the process nonuniformity and limitations in reproducibility. The refractive indices of core and cladding layers can have nonuniformities of up to $\pm 3 \times 10^{-4}$ in refractive index, and the core layer can show thickness variations up to $\pm 0.5\%$ over the wafer. The waveguide width can vary by ± 0.1 μm. The refractive index was measured by the prism-coupling method from a 7 cm $\times$ 7 cm area of a 4-in wafer, which is the useful area for device fabrication. The reproducibility in thickness is $\pm 1.2\%$ and in refractive index is $\pm 1.5 \times 10^{-3}$, which is within the measurement error.

The simulation results of the effects of these process-dependent deviations are summarized in Table III. A uniform change in effective refractive index emerges as a spectral shift in the transmission spectrum and a nonuniform change increases the overall crosstalk level. Although for both devices the maximum resulting variation of the effective refractive index of the waveguiding channel is low, an AWG is a very sensitive device and even small changes could lower the performance of the device dramatically. Variations in the core layer thickness and the waveguide width result in larger spectral shifts and crosstalk values compared to variations in core and cladding refractive indices, which are negligible.

By exploiting the thermo-optic (TO) effect of SiON, the shift in central wavelength of the transmission spectrum can be easily compensated by heating the whole chip. The TO coefficient of SiON is reported as 2.35×10^{-5}/K in [32]. Thus, a temperature rise of 5 K, for example, will increase the refractive index by $\Delta n \sim 10^{-4}$.

As a proof of concept, the TO effect was investigated only for the 1300-nm AWG, since the TO coefficient and the corresponding relative temperature-induced wavelength shift have the same order of magnitude for the 800- and 1300-nm wavelength ranges. Fig. 8 shows the temperature-induced shift of the central wavelength of the AWG in the temperature range of 0–30 K.

We observe that the device exhibits a wavelength shift of 0.65 nm for 30 K of temperature change, i.e., a shift rate of 0.022 nm/K. With this shift rate, the experimental TO coefficient

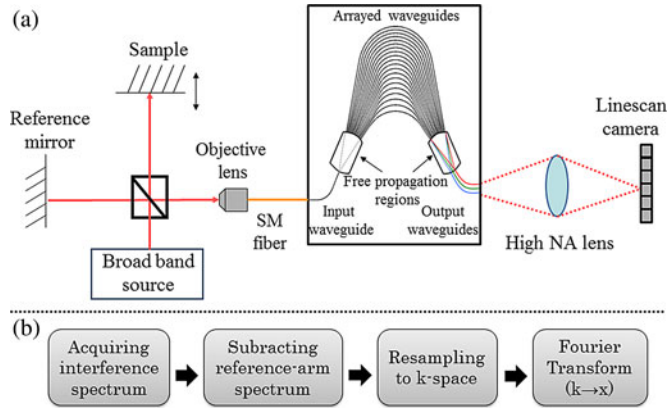

Fig. 9. (a) Optical measurement setup of the SD-OCT system with free-space MI and integrated AWG spectrometer. (b) Signal processing steps for SD-OCT.

of SiON was obtained as 2.06×10^{-5}/K, which agrees well with the theoretical value.

The increase in crosstalk, also indicated in Table III, reduces the device performance. Moreover, compensation of this type of performance degradation is not very easy or not even feasible. The fluctuations in the waveguide width and thickness of the core layer result in significant increments in the crosstalk levels of both devices. The tolerance analysis reveals that for a high-performance AWG, we need not only a good design but also a very good fabrication facility that provides waveguides with an effective refractive index within a tolerance lower than 10^{-4} in order to keep the shift in the transmission spectrum and the change in crosstalk lower than 0.2 nm and 2 dB for both devices, respectively.

The fiber-to-chip coupling loss was estimated to be about 3.5 and 5.5 dB/facet for the 800- and 1300-nm waveguides, respectively. This loss is mainly due to the difference in core size between the waveguides and the optical fibers. However, it is possible to reduce the coupling loss to 0.25 dB/facet by splicing the standard telecom fiber to a high-numerical aperture (NA) small-core fiber, as we have previously demonstrated [20]. As we only needed a temporary and quickly repositionable fiber-chip coupling for characterizing our devices, we can tolerate a relatively high coupling loss. Our present application does not require fiber-chip coupling.

IV. SD-OCT Measurements With AWG Spectrometers

A. Interferometric Distance Measurements

The schematic of the SD-OCT system with integrated AWG spectrometer is shown in Fig. 9(a). The measurement technique for the 800- and 1300-nm spectral ranges is similar, except for the different specifications of the light source (Superlum SLD-381-HP3 and Superluminescent B&W Tek, respectively) and the line scan camera (Dalsa, Spyder3 GigE and Sensors Unlimited, SU-LDH-1.7RT/LC, respectively).

The free-space Michelson interferometer (MI) is illuminated with a superluminescent diode emitting a partially polarized Gaussian-like spectrum with the specifications provided in Table IV. Light from the source is directed to the reference and sample arms by a 50:50 beam splitter. The reference mirror is kept stationary, while the sample mirror is moved during the experiments. Light returning from the two arms is focused by an objective lens into a single-mode fiber and directed to the AWG spectrometer. The output power of the MI is measured to be 0.1 and 0.9 mW for the 800- and 1300-nm spectral ranges, respectively. In the AWG spectrometer, the optical spectrum is dispersed by the arrayed waveguides and imaged by a camera lens (JML Optical, focal length: 50 mm) with high NA (NA = 0.5) onto the camera with the specifications provided in Table IV.

TABLE IV
Specifications of the Light Source and the Line Scan Camera for 800- and 1300-nm Measurements

Parameters		800 nm	1300 nm
Light source	Center wavelength	830 nm	1300 nm
	Bandwidth (FWHM)	13 nm	40 nm
	Output power	5 mW	7 mW
Linescan camera	Number of pixels	2048	1024
	Pitch of pixels	14 μm	25 μm
	Readout rate	36 kHz	46 kHz

Each line scan camera is operated at a readout rate for which the maximum optical power is close to the saturation limit of the camera (see Table IV). The raw unprocessed interference data are stored in memory at 25 frames/s. The acquired spectra are processed by subtracting the reference-arm spectrum and resampling to *k*-space, as indicated in Fig. 9(b). The reflectivity depth profile is obtained by performing a Fourier transformation of the digitized camera output. The measured spectra have an absolute wavelength scale defined by the center wavelength and FSR value of the AWG. The corresponding depth axis is calculated using (2).

B. Results and Discussion

The spectra shown in Fig. 10(a) and (b) are the spectra from the reference arm at 800 and 1300 nm, respectively. The optical bandwidths $\Delta\lambda_{\mathrm{FWHM}}$ of the spectra are measured as 12 and 39 nm for the 800- and 1300-nm AWG, respectively. These values correspond to an axial resolution of $\Delta z = 24$ and 19 μm, in agreement with the targeted axial resolution for 800 and 1300 nm, respectively. The insets show measured interference spectra after background subtraction, measured at a depth of 200 μm. The modulation on the spectra due to interference can be clearly observed.

The OCT signals measured for different depths, i.e., for different path length differences between sample and reference arm of the MI, are shown in Fig. 10(c) and (d). The depth scale corresponded one-to-one with the physical distance of the sample arm position change. We achieved imaging up to the maximum depth range of 1 mm for both wavelength ranges. The measured SNR was 75 dB at 100-μm depth for both wavelength bands, which includes 10-dB fiber-to-chip coupling loss, 7-dB free-space interferometer loss, and 5-dB chip-to-camera coupling losses. By reducing losses and increasing the output power of the light source, the sensitivity values of our SD-OCT systems

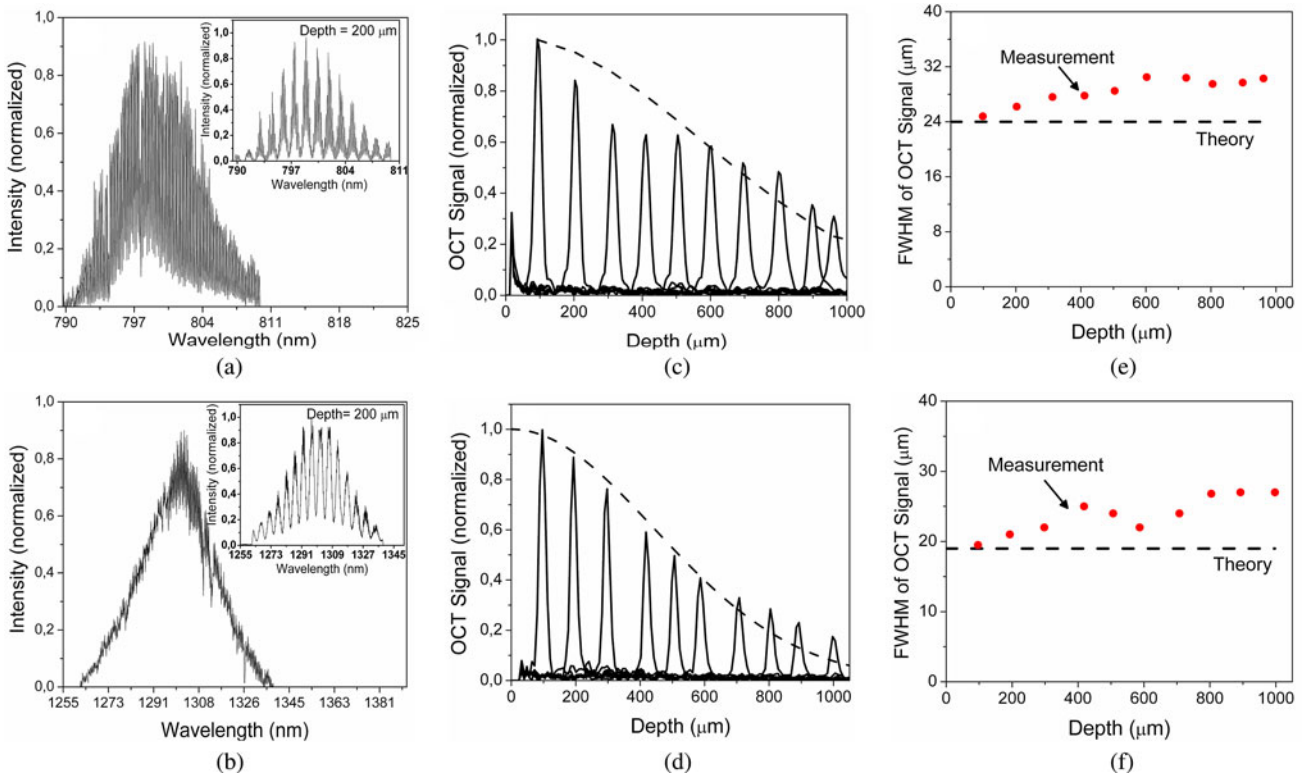

Fig. 10. Measured data for the 800- (upper row) and the 1300-nm AWG (lower row). (a) and (b) Measured reference spectra of the AWG spectrometers on the line scan cameras. The insets show interference spectra measured at 200-μm depth after background subtraction. (c) and (d) Measured OCT signal as a function of depth for a mirror reflector and fit of the roll-off (dashed line). The maximum depth range is 1 mm. (e) and (f) Measured OCT axial resolution (solid circles) in comparison with the theoretical axial resolution (dashed line). A decrease in resolution occurs for larger depths.

using AWG spectrometers can be improved to the level of state-of-the-art OCT systems. The FWHM values of the point spread functions at various depths are plotted in Fig. 10(e) and (f). An experimental axial resolution of 25 and 20 μm at 100-μm depth was obtained for 800 and 1300 nm, respectively. A decrease in resolution was found for both AWG spectrometers at larger depths, which we attribute to limited spectral sampling resolution of the SD-OCT system to resolve high-frequency spectral interference modulations from deeper areas. Imaging aberrations due to the high-NA lens, noise, and reduced interpolation accuracy of the resampling process at higher fringe modulations are possible causes of the measured loss of spectral resolution.

Equation (7) was fitted to the signal decay data presented in Fig. 10(c) and (d), with ω as a free parameter and $k = 0.5$. The value for ω obtained from the fit is 0.9 and 1.4, which is higher than the expected lower limit of $\omega = 0.32$ and $\omega = 0.55$ for the 800- and 1300-nm AWG, respectively. The discrepancy between theory and experiment could arise due to misalignment in the experimental setup as well as lens aberrations which cause spectral broadening of the spot size on the line scan camera pixel (in addition to imaging errors in the focal plane of the second FPR). In addition, the AWG spectrometers were not designed to be polarization insensitive; hence, partial polarization of the light source could cause degradation in roll-off in depth.

Imaging of the spectrometer output plane onto the line scan camera pixel array was not straightforward, since the output waveguides have a very high exit NA and the AWG output

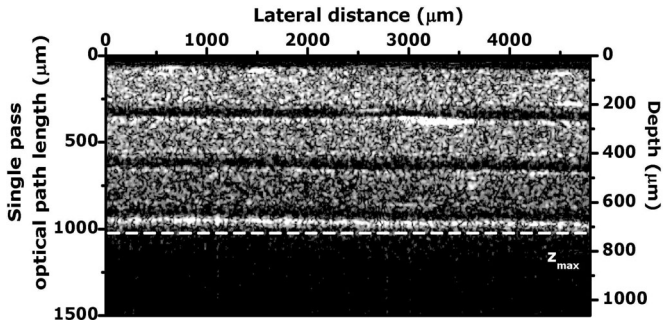

Fig. 11. OCT image of the three-layered scattering phantom measured with the AWG as spectrometer in SD-OCT. The dashed line indicates the maximum imaging depth. Reproduced from [16] with permission from the Optical Society of America.

channels are separated by 60 μm, resulting in a large collection area of a centimeter wide. Therefore, a high-NA camera lens is required to image the output-waveguide array on the edge of the chip onto the flat line scan camera imaging plane. Given the large field of view of the output-waveguide array and the high exit NA, we expect nonideal imaging performance over parts of the spectrum.

In our future work, the output channels of the AWG spectrometers will be separated by less than the current 60 μm to decrease the large collection area at the spectrometer output plane. In addition, we will integrate more optical components

necessary for OCT on a single chip to further reduce the OCT system footprint and costs.

As a demonstration of OCT cross-sectional imaging using the AWG spectrometer, an image of a three-layered scattering phantom is obtained by using part of a fiber-based OCT setup [33] with the AWG as spectrometer (see Fig. 11) [16].

As expected, all three scattering layers are observed up to the maximum single-pass optical path length of 1 mm (725-μm depth for the average refractive index of 1.38 of the phantom). The current imaging resolution and depth are sufficient for biological imaging but can be improved by increasing the FSR and the number of output channels.

V. Conclusion

We have designed, fabricated, and characterized SiON-based AWGs for the 800- and 1300-nm spectral regions with overall chip sizes of 2.6 cm $\times$ 2.1 cm and 3.0 cm $\times$ 2.5 cm, crosstalk values of -22 and -25 dB, excess loss values of 3.2 and 2.5 dB, and 3-dB bandwidths of 0.07 and 0.23 nm, respectively. In addition, we demonstrated the applicability of such AWGs for SD-OCT systems by performing interferometric depth-ranging measurements. An imaging depth of 1 mm and axial resolution of 25 and 20 μm (at 100-μm depth) are obtained for 800 and 1300 nm, respectively. The measurement results are in good agreement with the theoretical calculations. Furthermore, a phantom image was taken by using a fiber-based SD-OCT setup with the 1300-nm AWG spectrometer. By integrating one of the most challenging parts of the SD-OCT system onto a chip, we have moved a significant step forward toward on-chip SD-OCT systems.

Acknowledgment

The authors would like to thank D. Faber for supplying the Dalsa line scan camera and A. Hollink for technical support.

References

[1] D. Huang, E. A. Swanson, C. P. Lin, J. S. Schuman, W. G. Stinson, W. Chang, M. R. Hee, T. Flotte, K. Gregory, C. A. Puliafito, and J. G. Fujimoto, "Optical coherence tomography," *Science*, vol. 254, no. 5035, pp. 1178–1181, Nov. 1991.

[2] A. F. Fercher, C. K. Hitzenberger, G. Kamp, and S. Y. Elzaiat, "Measurement of intraocular distances by backscattering spectral interferometry," *Opt. Commun.*, vol. 117, no. 1–2, pp. 43–48, May 1995.

[3] D. X. Hammer, "Advances in retinal imaging," in *Advances in Optical Imaging for Clinical Medicine*, N. Iftimia, W. R. Brugge, and D. X. Hammer, Eds. Hoboken, NJ: Wiley, 2011, pp. 85–161.

[4] B. Cense, N. Nassif, T. Chen, M. Pierce, S.-H. Yun, B. Park, B. Bouma, G. Tearney, and J. de Boer, "Ultrahigh-resolution high-speed retinal imaging using spectral-domain optical coherence tomography," *Opt. Exp.*, vol. 12, no. 11, pp. 2435–2447, May 2004.

[5] R. Leitgeb, W. Drexler, A. Unterhuber, B. Hermann, T. Bajraszewski, T. Le, A. Stingl, and A. Fercher, "Ultrahigh resolution Fourier domain optical coherence tomography," *Opt. Exp.*, vol. 12, no. 10, pp. 2156–2165, May 2004.

[6] M. Wojtkowski, V. Srinivasan, T. Ko, J. Fujimoto, A. Kowalczyk, and J. Duker, "Ultrahigh-resolution, high-speed, Fourier domain optical coherence tomography and methods for dispersion compensation," *Opt. Exp.*, vol. 12, no. 11, pp. 2404–2422, May 2004.

[7] B. Potsaid, I. Gorczynska, V. J. Srinivasan, Y. Chen, J. Jiang, A. Cable, and J. G. Fujimoto, "Ultrahigh speed spectral/Fourier domain OCT ophthalmic imaging at 70000 to 312500 axial scans per second," *Opt. Exp.*, vol. 16, no. 19, pp. 15149–15169, Sep. 2008.

[8] B. Potsaid, B. Baumann, D. Huang, S. Barry, A. E. Cable, J. S. Schuman, J. S. Duker, and J. G. Fujimoto, "Ultrahigh speed 1050 nm swept source/Fourier domain OCT retinal and anterior segment imaging at 100000 to 400000 axial scans per second," *Opt. Exp.*, vol. 18, no. 19, pp. 20029–20048, Sep. 2010.

[9] S. Bourquin, P. Seitz, and R. P. Salathé, "Optical coherence tomography based on a two-dimensional smart detector array," *Opt. Lett.*, vol. 26, no. 8, pp. 512–514, Apr. 2001.

[10] S. Bourquin, L. Laversenne, S. Rivier, T. Lasser, R. P. Salathé, M. Pollnau, C. Grivas, D. P. Shepherd, and R. W. Eason, "Parallel broadband fluorescent light source for optical coherence tomography," in *Proc. SPIE, Coherence Domain Opt. Methods Opt. Coherence Tomogr. Biomed. IX*, vol. 5690, San Jose, CA, 2005, pp. 209–213.

[11] D. Culemann, A. Knuettel, and E. Voges, "Integrated optical sensor in glass for optical coherence tomography," *IEEE J. Sel. Topics Quantum Electron.*, vol. 6, no. 5, pp. 730–734, Oct. 2000.

[12] E. Margallo-Balbas, M. Geljon, G. Pandraud, and P. J. French, "Miniature 10 kHz thermo-optic delay line in silicon," *Opt. Lett.*, vol. 35, no. 23, pp. 4027–4029, Dec. 2010.

[13] G. Yurtsever, P. Dumon, W. Bogaerts, and R. Baets, "Integrated photonic circuit in silicon on insulator for Fourier domain optical coherence tomography," in *Proc. SPIE, Opt. Coherence Tomography Coherence Domain Opt. Methods Biomed. XIV*, vol. 7554, San Francisco, CA, 2010, pp. 1–5.

[14] V. D. Nguyen, N. Ismail, F. Sun, K. Wörhoff, T. G. van Leeuwen, and J. Kalkman, "SiON integrated optics elliptic couplers for Fizeau-based optical coherence tomography," *IEEE J. Lightw. Technol.*, vol. 28, no. 19, pp. 2836–2842, Sep. 2010.

[15] D. Choi, H. Hiro-Oka, H. Furukawa, R. Yoshimura, M. Nakanishi, K. Shimizu, and K. Ohbayashi, "Fourier domain optical coherence tomography using optical demultiplexers imaging at 60000000 lines/s," *Opt. Lett.*, vol. 33, no. 12, pp. 1318–1320, Jun. 2008.

[16] V. D. Nguyen, B. I. Akca, K. Wörhoff, R. de Ridder, M. Pollnau, T. G. van Leeuwen, and J. Kalkman, "Spectral domain optical coherence tomography imaging with an integrated optics spectrometer," *Opt. Lett.*, vol. 36, no. 7, pp. 1293–1295, Apr. 2011.

[17] S. H. Yun, G. J. Tearney, J. F. de Boer, and B. E. Bouma, "Pulsed-source and swept-source spectral-domain optical coherence tomography with reduced motion artifacts," *Opt. Exp.*, vol. 12, no. 23, pp. 5614–5624, Nov. 2004.

[18] M. K. Smit and C. van Dam, "Phasar-based WDM-devices: Principles, design and applications," *IEEE J. Sel. Topics Quantum Electron*, vol. 2, no. 2, pp. 236–250, Jun. 1996.

[19] H. Takahashi, S. Suzuki, K. Kato, and I. Nishi, "Arrayed-waveguide grating for wavelength division multi/demultiplexer with nanometre resolution," *Electron. Lett.*, vol. 26, no. 2, pp. 87–88, Jan. 1990.

[20] K. Wörhoff, C. G. H. Roeloffzen, R. M. de Ridder, A. Driessen, and P. V. Lambeck, "Design and application of compact and highly tolerant polarization-independent waveguides," *IEEE J. Lightw. Technol.*, vol. 25, no. 5, pp. 1276–1282, May 2007.

[21] K. Wörhoff, E. J. Klein, M. G. Hussein, and A. Driessen, "Silicon oxynitride based photonics," in *Proc. 10th Anniversary Inter. Conf. Trans. Opt. Netw.*, Athens, Greece, 2008, pp. 266–269.

[22] B. Schauwecker, G. Przyrembel, B. Kuhlow, and C. Radehaus, "Small-size silicon-oxynitride AWG demultiplexer operating around 725 nm," *IEEE Photon. Technol. Lett.*, vol. 12, no. 12, pp. 1645–1646, Dec. 2000.

[23] L. Leick, K. Zenth, C. Laurent-Lund, T. Koster, L.-U. A Andersen, L. Wang, B. H. Larsen, L. P. Nielsen, and K. E. Mattsson, "Low loss, polarization insensitive SiON components," presented at the Opt. Fiber Commun. Conf., Los Angeles, CA, 2004, Paper MF40.

[24] T. Shimoda, K. Suzuki, S. Takaesu, M. Horie, and A. Furukawa, "Low-loss, compact wide-FSR-AWG using SiON planar lightwave technology," presented at the Opt. Fiber Commun. Conf., Atlanta, GA, 2003, Paper FJ1.

[25] A. A. Goncharov, S. V. Kuzmin, V. V. Svetikov, K. K. Svidzinskii, V. A. Sychugov, and N. V. Trusov, "Integrated optical demultiplexer based on the SiO_2–SiON waveguide structure," *Quantum Electron.*, vol. 35, no. 12, pp. 1163–1166, Sep. 2005.

[26] T. H. Lee, K. H. Tu, and C. T. Lee, "Novel structure of an arrayed-waveguide grating multiplexer with flat spectral response," *Microw. Opt. Technol. Lett.*, vol. 41, no. 6, pp. 444–445, Jun. 2004.

[27] W. J. Liu, Y. C. Lai, M. H. Weng, C. M. Chen, and P. H. Lee, "Simulation and fabrication of silicon oxynitride array waveguide grating for optical communication," in *Proc. SPIE, Opt. Compon. Mater. II*, Apr. 2005, vol. 5723, pp. 43–54.

[28] E. A. Swanson, D. Huang, M. R. Hee, J. G. Fujimoto, C. P. Lin, and C. A. Puliafito, "High-speed optical coherence domain reflectometry," *Opt. Lett.*, vol. 17, no. 2, pp. 151–153, Jan. 1992.

[29] G. Häusler and M. W. Lindner, "'Coherence radar' and 'spectral radar'—New tools for dermatological diagnosis," *J. Biomed. Opt.*, vol. 3, no. 1, pp. 21–31, Jan. 1998.
[30] Z. Hu, Y. Pan, and A. M. Rollins, "Analytical model of spectrometer-based two-beam spectral interferometry," *Appl. Opt.*, vol. 46, no. 35, pp. 8499–8505, Dec. 2007.
[31] S. H. Yun, G. J. Tearney, B. E. Bouma, B. H. Park, and J. F. de Boer, "High-speed spectral-domain optical coherence tomography at 1.3 μm wavelength," *Opt. Exp.*, vol. 11, no. 26, pp. 3598–3604, Dec. 2003.
[32] R. W. Chuang and Z. L. Liao, "2 $\times$ 2 thermo-optic silicon oxynitride optical switch based on the integrated multimode interference waveguides," *J. Electrochem. Soc.*, vol. 157, no. 2, pp. H149–H152, Dec. 2009.
[33] J. Kalkman, A. V. Bykov, D. J. Faber, and T. G. van Leeuwen, "Multiple and dependent scattering effects in Doppler optical coherence tomography," *Opt. Exp.*, vol. 18, no. 4, pp. 3883–3892, Feb. 2010.

B. Imran Akca received the B.Sc. degree from the Department of Electrical and Electronics Engineering and the M.Sc. degree from the Institute of Material Science and Nanotechnology both from Bilkent University, Ankara, Turkey, in 2006 and 2008, respectively. She is currently working toward the Ph.D. degree in the area of integrated optics in the Integrated Optical MicroSystems Group, MESA+ Institute for Nanotechnology, University of Twente, Enschede, The Netherlands.

Her research interests include designing integrated arrayed waveguide grating spectrometers for optical coherence tomography systems.

Van Duc Nguyen received the M.Sc. degree in physics from the University of Central Florida, Orlando, in 2008. He is currently working toward the Ph.D. degree in the Department of Biomedical Engineering and Physics, Academic Medical Center, University of Amsterdam, Amsterdam, The Netherlands.

His research interests include the usage of integrated optics in optical coherence tomography (OCT) and on functional OCT.

Jeroen Kalkman received the M.Sc. degree in experimental physics from the Vrije Universiteit Amsterdam, Amsterdam, The Netherlands, and the Ph.D. degree from the Institute for Atomic and Molecular Physics, Amsterdam, where he was involved in erbium-doped photonic materials.

After doing research for two years at Philips NatLab, Eindhoven, The Netherlands, he joined the Academic Medical Center, University of Amsterdam, Amsterdam, where he has been involved in optical coherence tomography, light tissue interactions, and integrated optics for healthcare applications.

Nur Ismail was born in Palermo, Italy, in 1977. He received the B.S. degree in electronic engineering from the University of Palermo, Palermo, Italy, in 2002, the M.S. degree in information technology and telecommunications from the Research Center for Electronics in Sicily, Monreale, Italy, in 2003, and the M.Sc. degree in photonics and optoelectronics from the University of Rome "Roma Tre," Rome, Italy, in 2006. He is currently working toward the Ph.D. degree in the Integrated Optical MicroSystems Group, MESA+ Institute for Nanotechnology, University of Twente, Enschede, The Netherlands.

Between 2003 and 2006, he was involved in the field of information technology in Rome, Italy.

Gabriël Sengo received the B.Sc. degree in applied physics from the Polytechnic of Enschede, Enschede, The Netherlands, in 1995.

After having been active in industry for a number of years, he joined as a Technician the Integrated Optical Micro Systems Group, MESA+ Institute for Nanotechnology, University of Twente, Enschede. He specializes in lithography and reactive ion etching.

Fei Sun received the M.S. degree in microelectronics from Xi'an Jiaotong University, Xi'an, China, and the Ph.D. degree in optoelectronics from the Institute of Semiconductors, Chinese Academy of Sciences, Beijing, China, in 2001 and 2006, respectively.

He is currently a Scientist at the Institute of Microelectronics, A$*$STAR, Singapore.

Alfred Driessen received the M.Sc. degree in experimental physics and the Ph.D. degree in quantum solids from the University of Amsterdam, Amsterdam, The Netherlands, in 1972 and 1982, respectively.

After a period as a Postdoctoral Researcher at Free University, Amsterdam, where he was involved in metal hydrides, he joined the Lightwave Devices Group, University of Twente, Enschede, The Netherlands, as an Associate Professor in 1988. His research field from then is integrated optics for optical communication and optical nonlinear devices. From 2003 to 2009, he was a Full Professor within the Integrated Optical Micro Systems Group, MESA+ Institute for Nanotechnology, University of Twente. He is the author or coauthor of more than 250 refereed journal and conference papers and three patents. His research interests include compact and complex nanophotonic structures that can be applied in sensing, communication, and spectroscopy.

Ton G. van Leeuwen studied physics at the University of Amsterdam, Amsterdam, The Netherlands, and received the Ph.D. degree from the Laboratory of Experimental Cardiology, University of Utrecht, Utrecht, The Netherlands, in 1993.

He is currently the Head of the Department of Biomedical Engineering and Physics, Academic Medical Center, University of Amsterdam, and a Professor in the Biomedical Photonic Imaging Group, MIRA Institute for Biomedical Technology and Technical Medicine, University of Twente, Enschede, The Netherlands. His research interests include the clinical application of biomedical optics.

Markus Pollnau received the M.Sc. degree from the University of Hamburg, Hamburg, Germany, in 1992, and the Ph.D. degree from the University of Bern, Bern, Switzerland, in 1996, both in physics.

After postdoctoral positions with the University of Southampton and the University of Bern, he was a Project and Research Group Leader with the Swiss Federal Institute of Technology, Lausanne, Switzerland. In 2004, he became a Full Professor and the Chair of the Integrated Optical MicroSystems Group, MESA+ Institute for Nanotechnology, University of Twente, Enschede, The Netherlands. He has contributed to more than 400 reviewed journal and international conference papers and six book chapters in the fields of crystal and thin-film growth, rare-earth-ion spectroscopy, solid-state and fiber lasers, and waveguide fabrication, devices, and applications.

Dr. Pollnau has held European, Swiss, and Dutch personal Fellowships and has obtained numerous National and European Research Grants. He has been involved in the organization of major international conferences, e.g., as a Program and General Co-chair of the Conference on Lasers and Electro-Optics (2006/2008) and the Conference on Lasers and Electro-Optics Europe (2009/2011), and served as the Topical Editor for the *Journal of the Optical Society of America B*.

Kerstin Wörhoff received the M.Sc. degree in optoelectronics from the Technical University of Bratislava, Bratislava, Slovakia, and the Ph.D. degree in applied physics from the University of Twente, Enschede, The Netherlands, in 1991 and 1996, respectively.

In 1996, she joined the Lightwave Devices Group (now Integrated Optical MicroSystems Group, MESA+ Institute for Nanotechnology), University of Twente, as a Postdoctoral Researcher, where since 2000 she has been an Assistant Professor. Her research interests include the field of active and passive silicon-based photonics technology, rare-earth-ion-doped devices, and optical waveguide design.

René M. de Ridder (M'94) was born in Amsterdam, The Netherlands, in 1950. He received the M.S. and Ph.D. degrees in electrical engineering from the University of Twente, Enschede, The Netherlands, in 1978 and 1988, respectively. His thesis was focused on sensitive thin-film magnetic-field sensors.

Since 1981, he has been a Lecturer and a Research Scientist at the University of Twente, where he is currently a member of the Integrated Optical MicroSystems Group, MESA+ Institute for Nanotechnology. In 1988, he was involved in research in integrated optical devices. A basis for his research in this field was laid during a half year of sabbatical leave at AT&T Bell Labs, Holmdel, NJ, in 1989. His research interests include photonic crystal structures and wavelength-selective devices for applications in sensing and communication.